SCIENCE CHINA
Chemistry

•ARTICLES•

April 2023 Vol.66 No.4: 1211–1220
https://doi.org/10.1007/s11426-022-1534-8

Covalency triggers high catalytic activity of amorphous molybdenum oxides for oxidative desulfurization

Juncong Zou[1,2], Yan Lin[1*] & Chunping Yang[1,2,3*]

[1]*College of Environmental Science and Engineering, Hunan University and Key Laboratory of Environmental Biology and Pollution Control (Hunan University), Ministry of Education, Hunan University, Changsha 410082, China;*
[2]*Guangdong Provincial Key Laboratory of Petrochemcial Pollution Processes and Control, and School of Environmental Science and Engineering, Guangdong University of Petrochemical Technology, Maoming 525000, China;*
[3]*School of Environmental and Chemical Engineering, Nanchang Hangkong University, Nanchang 330063, China*

Received October 22, 2022; accepted February 6, 2023; published online February 13, 2023

Oxidative desulfurization (ODS) is a promising technology to produce clean fuel with requiring superior catalysts to lower kinetic barriers. Although most ODS catalysts are based on crystalline transition-metal oxides (TMOs), extraordinary activity also can be achieved with amorphous TMOs. However, the origin of the remarkable catalytic activity of the amorphous TMOs remains greatly ambiguous. Here, we found the crucial role of Mo–O covalency in ruling the intrinsic catalytic activity of amorphous molybdenum oxides (MoO_x). Experimental and theoretical analysis indicated that the nonequivalent connectivity in the amorphous structure strongly enhanced Mo–O covalency, thereby increasing the content of electrophilic oxygen and nucleophilic molybdenum to favor the MoO_x–H_2O_2 interaction. With the boosted Mo–O covalency to improve the flexibility of the charge state, the amorphous MoO_x-based composite catalyst (PE-MoO_x/S-0.05) exhibited outstanding catalytic activity for ODS of fuel oil. The turnover frequency (TOF) value of the catalyst (18.63 h^{-1}) was almost an order of magnitude higher than that of most reported crystalline MoO_x/molecular sieve composite catalysts. The in-depth understanding of the origin of the amorphous TMOs activity for ODS provides a valuable reference for developing ODS catalysts.

amorphous, molybdenum oxide, oxidative desulfurization, covalency

Citation: Zou J, Lin Y, Yang C. Covalency triggers high catalytic activity of amorphous molybdenum oxides for oxidative desulfurization. *Sci China Chem*, 2023, 66: 1211–1220, https://doi.org/10.1007/s11426-022-1534-8

1 Introduction

Despite the growing popularity of new energy applications, fuel oil still accounts for more than 30% of the market and dominates global energy consumption. However, the utilization of sulfur-containing fuel oil will inevitably lead to various environmental pollution [1,2]. Therefore, in many countries and regions, strict international fuel standards have been implemented, limiting the sulfur content in fuel to below 10 ppm, which further expands the demand for ultra-low sulfur fuel production [3,4]. Oxidation desulfurization (ODS) has been considered as the most promising technology for deep desulfurization of sulfur-containing fuel due to its mild reaction conditions, high selectivity and desulfurization rate [5–7]. Nevertheless, the key barrier to efficient ODS is always the limited activity of catalysts. Consequently, the development of highly active catalysts is crucial for the realization of this technology.

To date, transition-metal oxides (TMOs) have been proven to be the most promising ODS catalysts for practical applications owing to their superiorities of low cost, easy availability and combinative stability and activity [8,9]. Meanwhile, the modification in the structure of TMOs could further improve their catalytic activity [10]. Several recent

---

*Corresponding authors (email: yangc@hnu.edu.cn; linyan@hnu.edu.cn)

© Science China Press 2023

results have exhibited that TMOs with amorphous or slightly crystalline character demonstrated higher ODS activities than crystalline TMOs [11,12]. The amorphous TMOs have been investigated by density functional theory (DFT) calculation [12,13], X-ray photoelectron spectroscopy (XPS) [11], Raman spectroscopy [12], and pyridine adsorption-FTIR spectroscopy [14], in multimodal approaches. Although extensive effort, the origin of high catalytic ODS activity of amorphous TMOs materials remains largely obscure. The lack of deep understanding of the relationship between the structure and activity of the amorphous TMOs will seriously hinder the development of improved ODS catalysts.

The local environment of TMOs and their physicochemical properties can govern catalytic ODS performance. For example, in the case of crystals, it has been confirmed that the nanoscale confinement [15,16], the surface area [17,18], the average oxidation state of transition metal [15,16], and the structural defect [5,18,19], have a great impact on the ODS performance of TMOs. However, in amorphous TMOs, it is a priori unclear that this picture from a crystal system is applied to an ultrasmall domain structure (below 5 nm) which contains distortions, defects and diversified short-range ordered structures. Therefore, it is essential to verify the influence of the above related parameters on the catalytic activity of amorphous TMOs, which is instrumental in the decipherment of potential active sites. Indeed, differently synthesized amorphous TMOs exhibit different catalytic activity [12,20]. From the fundamental point of view, the activity is generally related to the high-energy sites, where the local structure varies from the thermodynamically auspicious low-energy configuration [20,21]. Hence, to reveal the origin of the intrinsic activity of amorphous TMOs, it is critical to figure out the atomic and electronic structures capable of determining activity and how they promote the catalytic ODS activity.

In this work, we synthesized a series of molybdenum oxide (MoO_x)-based composite materials with different crystallinity (PE-MoO_x/S-M, PW-MoO_x/S-M, AE-MoO_x/S-M and AW-MoO_x/S-M). The MoO_x was selected owing to their good ODS activity of its crystalline structure, but there is no report on amorphous MoO_x as an ODS catalyst to the best of our knowledge. We first probed the effects of several relevant parameters on the ODS activity of amorphous MoO_x, and identified that the Mo oxidation state and the crystallinity were the key parameters responsible for the catalytic activity. X-ray absorption fine structure (XAFS) was carried out to detect the atomic local coordinates and electronic structure of the high-energy sites in amorphous MoO_x, and accordingly a theoretical model was established. The results of the density of states (DOS), Bader charge analysis and charge density difference demonstrated the strong Mo–O covalency in amorphous MoO_x, and uncovered the detailed way of greater Mo–O covalency reducing the electron transfer between Mo 4d and O 2p orbitals to increase the content of electrophilic O species and nucleophilic Mo species. Finally, the synergistic effect of electrophilic O species and nucleophilic Mo species on enhancing the ODS activity of amorphous MoO_x was deciphered.

2 Results and discussion

2.1 Crystallinity of catalysts

To confirm the crystallinity of MoO_x within the composite materials, the crystal structures were probed by high-resolution transmission electron microscopy (HRTEM) and selected area electron diffraction (SAED), respectively. As shown in Figure 1a–c, no lattice fringes were observed in HRTEM images of PE-MoO_x/S-0.05, PW-MoO_x/S-0.05 and AE-MoO_x/S-0.05, demonstrating their amorphous nature. This was further verified by the SAED patterns, which displayed a typical halo around the central highlight for amorphous materials (inset). Instead, the HRTEM image of AW-MoO_x/S-0.05 presented small crystalline domains of less than 5 nm (Figure 1d), and the corresponding SAED pattern indicated a slightly blurred array of diffraction dots. The results jointly revealed the short-range ordered structure of the MoO_x in AW-MoO_x/S-0.05 (Figure 1d, inset). The above results indicated that ethylene glycol and phosphomolybdic acid were conducive to the formation of amorphous MoO_x. This behavior was further confirmed by X-ray diffraction (XRD) analysis for MoO_x/S-0.15 serial catalysts. As shown in Figure 4a, AW-MoO_x/S-0.15, AE-MoO_x/S-0.15, PW-MoO_x/S-0.15 and PE-MoO_x/S-0.15 demonstrated gradually reduced crystallinity of 37.85%, 28.84%, 12.47% and 1.36%, respectively.

2.2 Oxidative desulfurization performance of catalysts

To evaluate the catalytic activity of amorphous MoO_x, MoO_x/S-0.05 catalysts synthesized *via* different methods were applied for ODS under fixed reaction conditions. As shown in Figure 2a, AW-MoO_x/S-0.05 demonstrated unsatisfactory ODS activity, and only 60.04% removal of DBT was obtained even after 60 min of reaction. Compared with AW-MoO_x/S-0.05, AE-MoO_x/S-0.05, PW-MoO_x/S-0.05 and PE-MoO_x/S-0.05 exhibited higher DBT removal efficiency. In particular, PE-MoO_x/S-0.05 showed the best ODS catalytic activity, with 100% DBT removal in 60 min. To give a deep insight into the catalytic process of different samples, the apparent rate constants (*k*) and turnover frequencies (TOFs) of different catalysts were further analyzed (Figure 2b, Figure S3). The apparent rate constant of DBT oxidation on PE-MoO_x/S-0.05 was 0.067 min^{-1}, which was 6.7 times higher than that of AW-MoO_x/S-0.05 (0.010 min^{-1}). Simi-

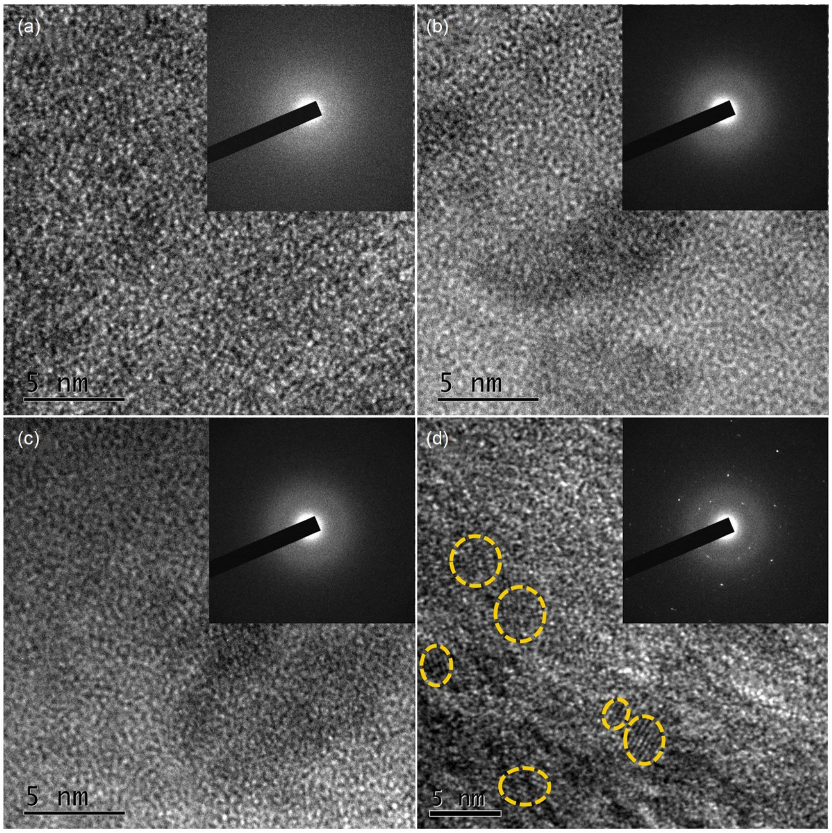

Figure 1 Structure characterization of MoO_x/S-0.05 serial catalysts. HRTEM and corresponding SAED images of (a) PE-MoO_x/S-0.05, (b) PW-MoO_x/S-0.05, (c) AE-MoO_x/S-0.05 and (d) AW-MoO_x/S-0.05 (color online).

larly, the TOF value (14.13 h^{-1}) of AW-MoO_x/S-0.05 was lower than that of all other evaluated catalysts. Importantly, to emphasize the robust catalytic activity of amorphous MoO_x, we summarized almost all the ODS reactions of DBT on crystalline MoO_x/molecular sieve composite materials in recent years (Figure 2c, Table S2). It is also worth reminding that the selected ODS reactions were carried out in the same system (H_2O_2 as the oxidant and acetonitrile as the extractant) for better comparison. It can be found that most of the composite catalysts exhibited good ODS activity at 333–353 K, but their activities were still lower than that of PE-MoO_x/S-0.05. Noticeably, the TOF value of PE-MoO_x/S-0.05 attained 18.63 h^{-1} at 333 K, which was almost an order of magnitude higher than that of most reported catalysts.

In addition, to further investigate the high catalytic activity of amorphous MoO_x, we also measured the activity of MoO_x/S-0.15 series catalysts, and the results were shown in Figure S4. It could be clearly seen that the catalytic activity of MoO_x/S-0.15 catalysts decreased with the rank of PE-MoO_x/S-0.15>PW-MoO_x/S-0.15>AE-MoO_x/S-0.15>AW-MoO_x/S-0.15. The results were extremely similar to those of the MoO_x/S-0.05 series catalysts. The above results indicated that the most active catalysts in each series were acquired *via* using phosphomolybdic acid as the Mo precursor and ethylene glycol as the solvent, more crystalline catalyst of each series being systematically less active. Overall, the catalytic activity of amorphous MoO_x could be influenced by several parameters, which will be studied and discussed in detail in the following sections.

2.3 Possible influence of nanoscale confinement and surface area

Previous literature clarified that the nanoscale spatial confinement has the potential to heighten the local concentration of thiophene compounds in the environment where the active site is located, thereby enhancing the ODS activity [16]. Furthermore, as presented in Figure S5, based on the Fick's law, the steep concentration gradient (vertical to the stream direction) in the nanoscale space can provide the driving force for oxidant and organic molecules from the center to the boundary [22,23]. The rapid mass transfer boosts the activation efficiency between oxidant and active sites. Meanwhile, contaminants in close vicinity to the active site have more opportunities to be attacked by pro-electronic intermediates.

To verify the possible role of nanoscale spatial confinement on the enhancement of the catalytic activity of Mo oxides, we explored the distribution of Mo oxides on the support by TEM. TEM images of PE-MoO_x/S-0.05, PW-

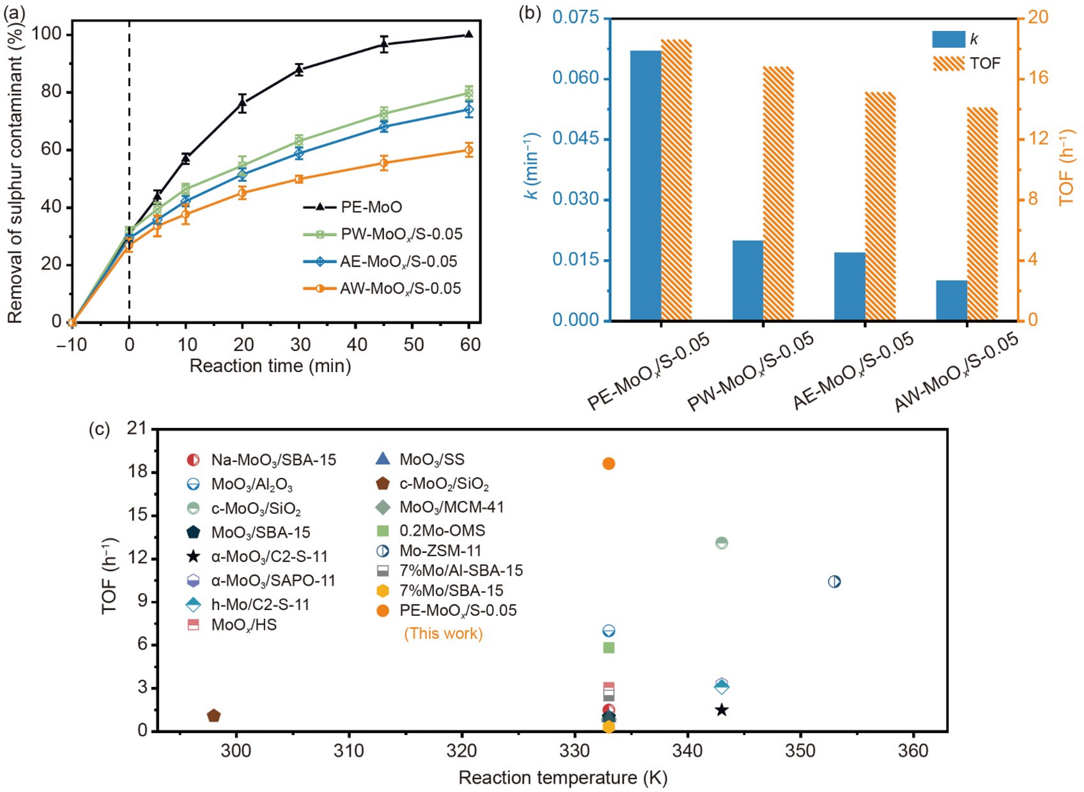

Figure 2 Oxidative desulfurization performance of the catalysts. (a) DBT conversion *vs*. reaction time with MoO$_x$/S-0.05 catalysts. (b) Catalytic activity of MoO$_x$/S-0.05 catalysts for– the oxidation of DBT. (c) Comparison of TOF values with the crystalline MoO$_x$/molecular sieve composite catalysts reported in literature (see supporting information in detail). Reaction conditions: 50 mg catalyst, 15 mL model fuel, 5 mL acetonitrile, O/S molar ratio of 4 and 333 K (color online).

MoO$_x$/S-0.05 and AW-MoO$_x$/S-0.05 clearly showed that Mo oxide nanoparticles were uniformly confined in the channels of ordered mesoporous SBA-15 (Figure 3a, b, d). On the contrary, since the EG cannot dissolve ammonium molybdate, it acts as a barrier layer, further preventing the diffusion of Mo precursors into the mesoporous SBA-15. Therefore, no Mo oxide nanoparticle was found in the mesoporous channels of AE-MoO$_x$/S-0.05 (Figure 3c). Moreover, only in the TEM images of AE-MoO$_x$/S-0.05, some larger Mo oxide particles were observed outside the pores of SBA-15 (Figure S6). For all the samples, it can be verified that there was no nanoscale spatial confinement effect to Mo oxides in only AE-MoO$_x$/S-0.05, while the ODS activity of AE-MoO$_x$/S-0.05 was not the lowest. The results clarified that the nanoscale confinement was not the primary parameter to explain the origin of the most active ODS catalyst.

Additionally, to obtain a better insight into the textural properties of the materials, physisorption measurements for various samples were performed, and the data are presented in Table S3 and Figure S7a, b. Compared with SBA-15, the pore size of AE-MoO$_x$/S-0.05 demonstrated an insignificant reduction, indicating that Mo oxides were distributed outside the pores, which is consistent with the results of TEM. It is worth reminding that for composite materials with almost the same Mo content, BET surface area is an excellent indicator to confirm whether the decrease or increase of activity may be the result of the change of the surface area of the catalyst. Therefore, we probed the intrinsic activity (ln$k$) of each material as a function of BET surface area and examined whether there was a correlation between surface area and ODS activity of the material (Figure S7c). The results showed that there was no significant correlation between the BET surface area of the composite catalyst and ln$k$. Consequently, the increase or decrease of surface area could not be responsible for explaining the higher or lower activity of the catalyst.

2.4 Possible influence of crystallinity and Mo oxidation state

Since the location and dispersion of amorphous MoO$_x$ could not elucidate the origin of superior ODS activity, we investigated their crystal structure and oxidation state. Considering that the contents of MoO$_x$ in MoO$_x$/S-0.05 series catalysts were lower than the detection limit of XRD technology (Figure S8), we chose MoO$_x$/S-0.15 series catalysts as the object to process XRD analysis for better presenting the results. As shown in Figure 4a, the crystallinity of Mo oxides in MoO$_x$/S-0.15 series catalysts augmented in the rank of PE-MoO$_x$/S-0.15<PW-MoO$_x$/S-0.15<AE-MoO$_x$/S-0.15<

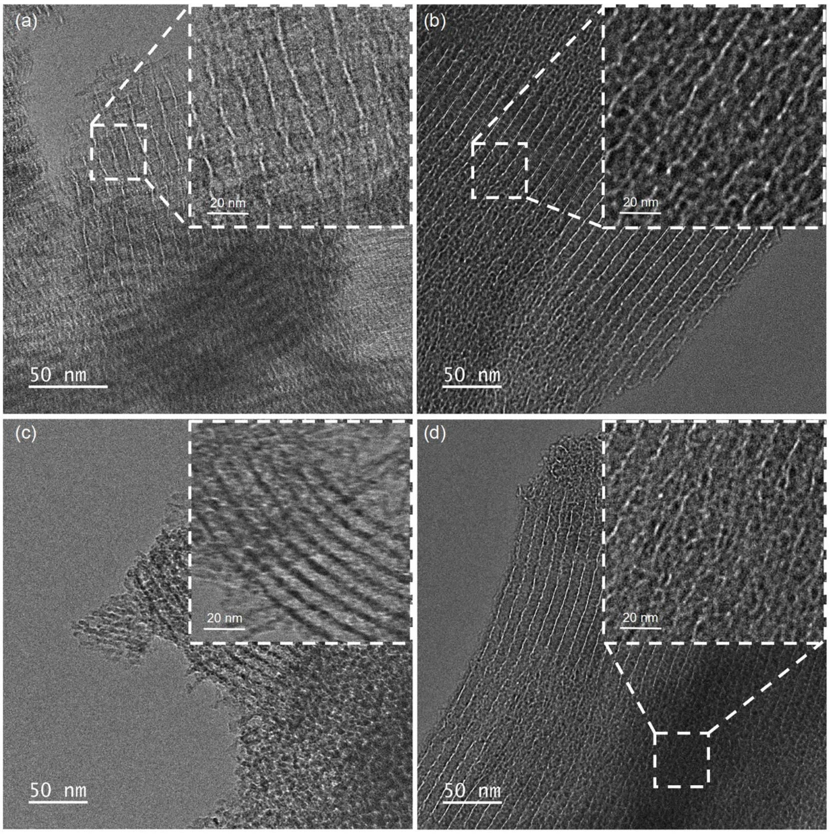

Figure 3 Morphology of the catalysts. TEM images of (a) PE-MoO$_x$/S-0.05, (b) PW-MoO$_x$/S-0.05, (c) AE-MoO$_x$/S-0.05 and (d) AW-MoO$_x$/S-0.05.

AW-MoO$_x$/S-0.15, which was reverse to that of catalytic activity. These results suggested that the long-range ordered structure of Mo oxides was detrimental to the catalytic reaction. Moreover, a highly negative correlation between the catalytic activity and the crystallinity of MoO$_x$/S-0.15 series catalysts further supported the above conclusions (Figure 4c). Given the above, it can be determined that crystallinity played a dominant role in governing the intrinsic catalytic activity of amorphous MoO$_x$.

X-ray photoelectron spectroscopy (XPS) was performed to analyze the specific valence state distribution of Mo in catalysts (Figure 4b, Figure S9). The existence of Mo^{V} (232.3±0.2 eV) and Mo^{VI} (233.5±0.3 eV) could be observed in all catalysts (Table S4). The oxidation state of Mo oxides can be represented by the atomic ratio of Mo^{V} to Mo^{VI} [10, 24]. It can be found that the atomic ratios of Mo^{V} to Mo^{VI} in the two series of materials decreased with the order of PE-MoO$_x$/S>PW-MoO$_x$/S>AE-MoO$_x$/S>AW-MoO$_x$/S, which was consistent with that of catalytic activity, suggesting that the catalysts with higher activity exhibited lower Mo oxidation state (Table S1). Importantly, a high correlation was established between ln$k$ and Mo^{V}/Mo^{VI} ratio (Figure 4d, Figure S10), which implied that the strengthening of activity in the amorphous MoO$_x$ could be attributed to the decrease of the Mo oxidation state. Besides, this conclusion was further confirmed by the XPS analysis of the used PE-MoO$_x$/S-0.05 (Figure S11), where the content of Mo^{V} in the catalyst diminished by 20.68% after reaction (Table S1).

Interestingly, the binding energies of Mo 3d in other samples shifted toward higher energies than that of AW-MoO$_x$/S catalysts (Table S4). This similar phenomenon has also been reported in previous studies, which is due to the increase of the average electronegativity of Mo atoms or the decrease of the distance from the nearest neighbors with the enhancement of the disorder degree of Mo oxides structure in the composites [10,25]. The higher electronegativity of Mo or the shorter distance between Mo and O is positive for the improvement of Mo–O covalency, further resulting in the generation of Mo^{V}. Given that the reduction in the Mo oxidation state may be the result of enhanced Mo–O covalency triggered by aggravated structural disorder in the Mo oxide, it can be speculated that the high catalytic activity of the amorphous MoO$_x$ can be correlated to the strong Mo–O covalency resulting from the hybridization between Mo 4d and O 2p orbitals.

2.5 Investigation of Mo–O covalency in amorphous Mo oxides

To further probe the local structure and the chemical state of

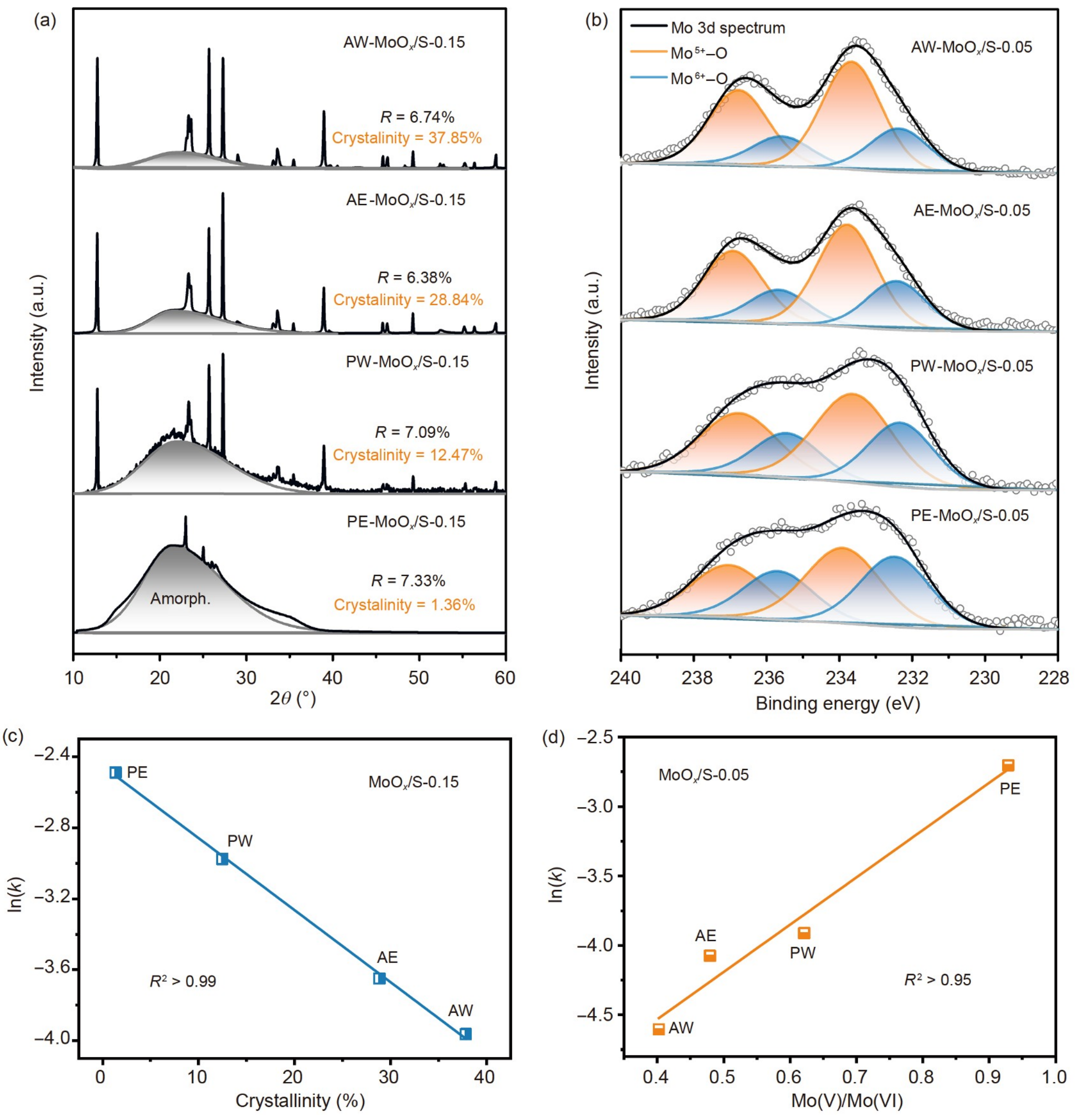

Figure 4 Crystallinity and molybdenum oxidation state are key parameters affecting catalytic activity. (a) XRD patterns and calculated crystallinity from XRD analysis. Gray gradient regions represent the area under the diffraction pattern associated with the amorphous (amorph., glass) component from 10–40° of 2*θ*. (b) High-resolution XPS spectrum of Mo 3d for MoO_x/S-0.05 composites. (c) Correlations between ln*k* and crystallinity. (d) Correlations between ln*k* and Mo oxidation state (color online).

Mo in amorphous MoO_x, X-ray absorption near-edge structure (XANES) and extended x-ray absorption fine structure (EXAFS) analyses were performed. In the Mo *K*-edge XANES, similar to MoO_3, AW-MoO_x/S-0.05 and PE-MoO_x/S-0.05 also demonstrated shoulder peaks (■) in the pre-edge region, indicating that the average oxidation state of Mo in AW-MoO_x/S-0.05 and PE-MoO_x/S-0.05 was close to 6 (Figure 5a). Furthermore, based on the positive correlation between the peak energy in the first-derivative curve and the oxidation state of Mo [26,27], it can be observed that the oxidation state of Mo in PE-MoO_x/S-0.05 was lower than that in AW-MoO_x/S-0.05 (Figure S12). These results are consistent with those of the above XPS. The Fourier transform-EXAFS is shown in Figure 5b. AW-MoO_x/S-0.05 and PE-MoO_x/S-0.05 mainly exhibited strong peaks around 1.34 Å, which was attributed to the Mo–O scattering path. Noticeably, the intensity of the typical long-range ordered peaks (Mo–O–Mo) diminished in the order of MoO_3≈MoO_2>AW-MoO_x/S-0.05>PE-MoO_x/S-0.05, indicating that the degree of the disorder increased in turn, while PE-MoO_x/S-0.05 exhibited the lowest crystallinity [10]. The results agree well with the aforementioned HRTEM and SAED observations. To identify the adjacent properties of Mo atoms, wavelet transform (WT)-EXAFS was carried out. As displayed in Figure 5c and d, the intensity maximum in WT contour plots for AW-MoO_x/S-0.05 and PE-MoO_x/S-0.05 was located at 6.52 and 6.90 $Å^{-1}$, respectively, corresponding to the Mo–O coordination. Moreover, the Mo–O bond in PE-MoO_x/S-0.05 was shorter than that in AW-MoO_x/S-0.05, which is in good agreement with the XPS results.

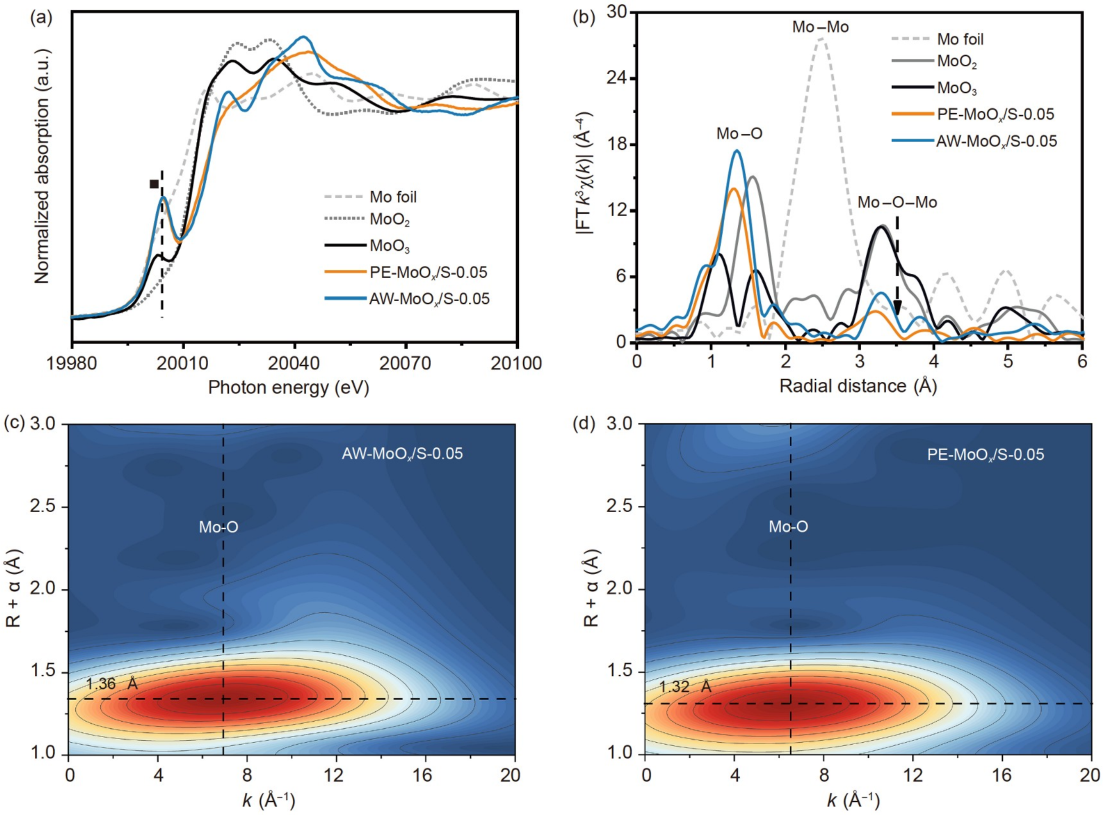

Figure 5 X-ray absorption characterization. (a) XANES and (b) Fourier transform (FT) EXAFS spectra, of AW-MoO$_x$/S-0.05, PE-MoO$_x$/S-0.05 and the reference samples at Mo *K*-edge. Wavelet transform of the k^3-weighted EXAFS data of (c) AW-MoO$_x$/S-0.05 and (d) PE-MoO$_x$/S-0.05 at Mo *K*-edge (color online).

Combining the chemical state with the corresponding structural characterizations, it can be determined that the structure of MoO$_x$ in the composite catalyst was similar to that of amorphous MoO$_3$. Consequently, to establish the approximate atomic model of amorphous MoO$_x$ (*a*-MoO$_x$), we performed molecular dynamics (MD) calculations on crystalline MoO$_3$ (*c*-MoO$_x$) including 144 atoms according to melting and quenching methods (Figure S13) [28,29]. The partial radial distribution function was then calculated and plotted (Figure 6a). For the *a*-MoO$_x$, the representative $g(r)$ peaks (illustrated by the vertical dashed lines) indicated that the average bond lengths of Mo–O, O–O and Mo–Mo bond pairs were 1.78, 2.71 and 3.89 Å, respectively, which are consistent with the quantitative EXAFS fitting data of the Mo–O bond distance of 1.77 and 1.79 Å (Figure S14, Table S5). Compared with the $g(r)$ peaks in *c*-MoO$_x$, the long-range ordering of more than 4 Å in the *a*-MoO$_x$ was significantly reduced. Moreover, the Mo–O bond length was slightly shortened, meaning the enhanced Mo–O covalency, which agrees well with the results of XPS and WT-EXAFS. As a result, the generated ultra-large *a*-MoO$_x$ supercell (~3 nm) was appropriate for modeling amorphous Mo oxides.

To reveal the influence and relationship of charges of Mo and O atoms and the related structural motifs, the population histograms for the Bader charge of Mo and O atoms in *a*-MoO$_x$ and *c*-MoO$_x$ were calculated, respectively (Figure 6b). For the *c*-MoO$_x$, the calculated Bader charge of Mo atom was +2.60*e*, while that of Mo atoms in the *a*-MoO$_x$ was lower and determined between +2.35 to +2.47*e*. After turning to the atomic charges of O atoms, it can be found that the negative Bader charge values in the *c*-MoO$_x$ were between −1.01 to −0.92 and −0.67 to −0.66*e*. The corresponding values of O atoms in the *a*-MoO$_x$ were between −0.99 to −0.85 and −0.60 to −0.52*e*. Obviously, the charge state ranges of Mo and O atoms in the *a*-MoO$_x$ were more flexible, which is attributed to the serious local structural disorder and distortion [20]. In addition, the wider variation of Bader charges of Mo atoms in the *a*-MoO$_x$ suggested the probable appearance of mixed valence states of Mo (Mo$^{\text{V}}$ and Mo$^{\text{VI}}$) [28]. It is worth noting that compared with those of *c*-MoO$_x$, O atoms in the *a*-MoO$_x$ were more electrophilic and Mo atoms were more nucleophilic (*i.e.*, smaller in absolute values of Bader charge).

The more electrophilic O species and nucleophilic Mo species in the *a*-MoO$_x$ were primarily triggered by boosted Mo–O covalency. The projected density of states (PDOS) showed that the overlap between Mo 4d and O 2p orbitals in the *a*-MoO$_x$ was significantly higher than that in the *c*-MoO$_x$, especially in the bonding orbital interval, which confirmed the stronger Mo–O covalency in amorphous Mo oxides (Figure 6c) [24]. In addition, the degree of Mo–O covalency

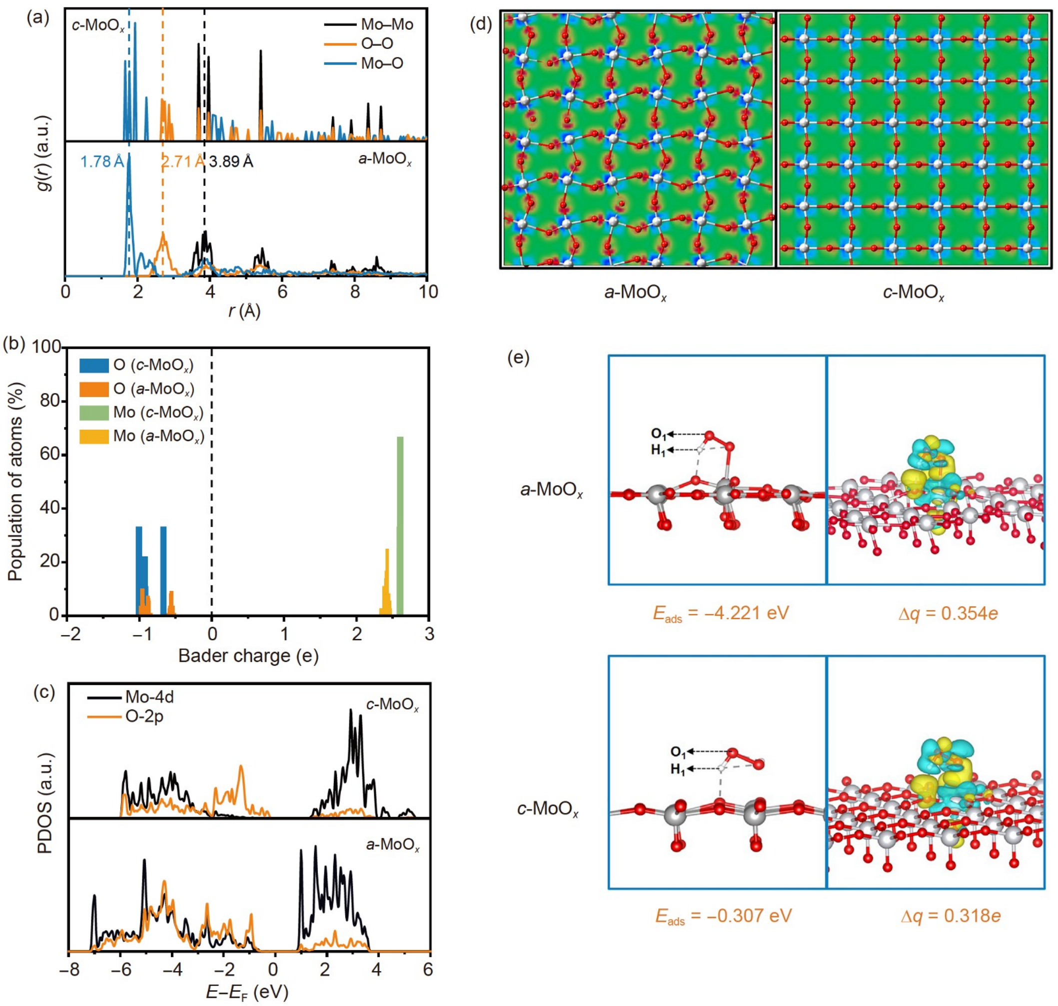

Figure 6 Geometric and electronic structure of crystalline and amorphous molybdenum oxides. (a) Partial radial distribution function (RDF, $g(r)$) for amorphous and crystalline Mo oxides. (b) The Bader charge histogram for O and Mo atoms in amorphous and crystalline Mo oxides. (c) The computed PDOS of Mo 4d, O 2p in amorphous and crystalline Mo oxides. (d) Charge density difference of Mo and O in amorphous and crystalline Mo oxides. The red and sky blue isosurfaces stand for the charge accumulation and depletion zones, respectively. (e) Representative models of adsorption and electronic interaction between amorphous or crystalline Mo oxides and H_2O_2. The yellow and sky blue isosurfaces in 3D charge density difference (with an isovalue of 0.0008e Å^{-3}) represent the charge accumulation and depletion zones, respectively (color online).

can be indicated by the charge deviation of O [30]. The higher the deviation was, the greater the possibility of electrons being dragged away from O atoms by Mo atoms, which led to stronger Mo–O covalency (Figure S15). To observe the charge distribution in Mo–O bonds in an intuitive way, the difference charge density was analyzed (Figure 6d). It can be clearly seen that more charges in *a*-MoO$_x$ were distributed on the Mo–O bond, implying that electrons in O were more inclined to polarize to Mo atoms and form a common electron group. Therefore, it can be concluded that the increase of electrophilic O species and nucleophilic Mo species in amorphous Mo oxides was ascribed to the pulling away of electrons from O atoms and the regression of charges to Mo atoms caused by the enhanced Mo–O covalency. Importantly, nucleophilic Mo species (Mo^{V}) are widely identified as driving forces for efficient ODS [5,15,17,31,32].

2.6 Mechanisms of Mo–O covalency governing the activity of amorphous Mo oxides

For the purpose of further uncovering the essential role of Mo–O covalency structure unit as the catalytic active site in amorphous Mo oxides, the interaction mechanism between Mo oxides and H_2O_2 was probed. Generally, adsorption energy (E_{ads}) governs the interaction between the catalyst and oxidant and reflects the thermodynamic feasibility of the adsorption process [33]. Thus, two optimized adsorption configurations of *c*-MoO$_x$/H_2O_2 and *a*-MoO$_x$/H_2O_2 are provided in Figure 6e. The E_{ads} of H_2O_2 increased from −0.31 (*c*-MoO$_x$) to −4.22 eV (*a*-MoO$_x$), implying that H_2O_2 was energetically preferred to coordinate with Mo–O bond in *a*-MoO$_x$. In addition, the length changes of chemical bonds in H_2O_2 before and after adsorption were calculated (Table S6). It can be seen that the bond length of only O$_1$–H$_1$ bond involved in coordination was significantly increased from 0.980 (original H_2O_2) to 0.995 (*c*-MoO_x) and 1.002 Å (*a*-MoO_x), respectively. The results suggested that Mo oxides tended to destroy the O_1–H_1 bond in H_2O_2 molecules, resulting in the generation of active species. Significantly, the considerable effect of Mo–O bond in *a*-MoO_x on H_2O_2 indicated that enhanced Mo–O covalency was more conducive to the dissociation of H_2O_2, which corresponds to our previous speculation.

To visualize the change of electron density distribution between H_2O_2 and Mo oxides, a 3D charge density difference analysis was carried out (Figure 6e). It is observed that the electron depletion region was mainly concentrated on the Mo atom and the H atom closest to the Mo oxides, while the electron accumulation region was distributed on the O atom (*c*-MoO_x and *a*-MoO_x) and the O atom (H_2O_2) nearest to the Mo oxides. The results revealed that the coordination impetus of H_2O_2 with the Mo–O bond in the Mo oxides was derived from the direct electron transfer between O and H atoms and between Mo and O atoms. Furthermore, the results of the Bader charge analysis showed that more electrophilic O species and nucleophilic Mo species facilitated the electron transfer between Mo oxides and H_2O_2 (Table S7). Evidently, the electrophilic O species and the nucleophilic Mo species in Mo oxides played an important synergistic role in the activation of the O–H bond in H_2O_2. Notably, our findings are not the same as previous reports that commonly focus on the contribution of the nucleophilicity of Mo atoms in the coordination process, while ignore the synergistic effect of the electrophilicity of O atoms.

In addition, according to the results of the radical trapping experiment, it can be determined that ·OH and $\cdot O_2^-$ were not the dominant active species in the ODS process (Figure S16). Given it, the possible ODS mechanism of amorphous Mo oxide was proposed as displayed in Figure S17. The ODS reaction over the amorphous Mo oxide could be divided into three steps. Firstly, the Mo–O bond and H–O–O structural unit formed a five-membered ring through the electron transfer, which led to the fracture of the O–H bond. Then, the S atom in DBT was attacked by the electrophilic oxygen species generated in step (1) to produce sulfoxide (DBTO). Finally, step (3) was similar to step (2), where DBTO was further oxidized to sulfone ($DBTO_2$). Especially, step (1) was considered to be the rate-determining step of ODS reaction, which was governed by Mo–O covalency.

3 Conclusions

The MoO_x-based composite catalyst with adjustable crystallinity could be obtained by the two-step annealing approach. Accordingly, we revealed the key role of Mo–O covalency in dominating the intrinsic catalytic activity of amorphous MoO_x. Compared with crystalline counterparts, the non-equivalent connectivity in amorphous MoO_x greatly enhanced the Mo–O covalency, thereby increasing the content of electrophilic oxygen and nucleophilic molybdenum, which was conducive to the MoO_x–H_2O_2 interaction. The optimized catalyst (PE-MoO_x/S-0.05) showed excellent catalytic activity for the ODS of fuel oil. The TOF value could reach 18.63 h^{-1}, almost one order of magnitude higher than that of most reported crystalline MoO_x/zeolite composite catalysts. Besides these important findings, this study also identified the crystallinity and Mo oxidation state as crucial parameters for the high ODS activity of amorphous MoO_x and ruled out the effects of nanoscale confinement and surface area. This work provides new insights into the origin of the outstanding catalytic activity of amorphous TMOs in ODS of fuels and may lay the foundation for the design of improved TMO catalysts.

Acknowledgements This work was supported by the National Natural Science Foundation of China (51978178, 52270064, and 51521006), the Department of Science and Technology of Guangdong Province of China (2022A1515010226), the Program for Innovative Research Teams of Guangdong Higher Education Institutes of China (2021KCXTD043), Key Laboratory of Petrochemical Pollution Control of Guangdong Higher Education Institutes (KLGHEI 2017KSYS004), the Science and Technology Innovation Program of Hunan Province of China (2021RC2058), and the Startup Fund of Guangdong University of Petrochemical Technology (2018rc63).

Conflict of interest These authors declare no conflict of interest.

Supporting information The supporting information is available online at chem.scichina.com and link.springer.com/journal/11426. The supporting materials are published as submitted, without typesetting or editing. The responsibility for scientific accuracy and content remains entirely with the authors

1 Lamonier C. *Nat Energy*, 2017, 2: 17019
2 Shafiq I, Hussain M, Rashid R, Shafique S, Akhter P, Yang W, Ahmed A, Nawaz Z, Park YK. *Chem Eng J*, 2021, 420: 130529
3 Ye G, Wang H, Chen W, Chu H, Wei J, Wang D, Wang J, Li Y. *Angew Chem Int Ed*, 2021, 60: 20318–20324
4 Hassan SU, Ahmad S, Farid MA, Nadeem S, Ali Z, Abro R, Mohyuddin A, Nazir MS, Hussain M, Park YK. *J Industrial Eng Chem*, 2022, 116: 438–446
5 Zou J, Lin Y, Wu S, Zhong Y, Yang C. *Adv Funct Mater*, 2021, 31: 2100442
6 Jiang W, An X, Xiao J, Yang Z, Liu J, Chen H, Li H, Zhu W, Li H, Dai S. *ACS Catal*, 2022, 12: 8623–8631
7 Shafiq I, Shafique S, Akhter P, Ishaq M, Yang W, Hussain M. *J Cleaner Production*, 2021, 294: 125731
8 He J, Wu P, Lu L, Li H, Ji H, He M, Jia Q, Hua M, Zhu W, Li H. *ACS Appl Mater Interfaces*, 2019, 11: 36666–36675
9 Yazdani S, Kashfi-Sadabad R, Huan TD, Morales-Acosta MD, Pettes MT. *Langmuir*, 2018, 34: 6296–6306
10 Elmaalouf M, Odziomek M, Duran S, Gayrard M, Bahri M, Tard C, Zitolo A, Lassalle-Kaiser B, Piquemal JY, Ersen O, Boissière C, Sanchez C, Giraud M, Faustini M, Peron J. *Nat Commun*, 2021, 12: 3935
11 Liu X, Liu X, Shan J, Huai J, Yang H, Yan X, Zheng Y, Li H. *InOrg Chem Commun*, 2021, 123: 108336

12 Palomeque-Santiago JF, López-Medina R, Oviedo-Roa R, Navarrete-Bolaños J, Mora-Vallejo R, Montoya-de la Fuente JA, Martínez-Magadán JM. *Appl Catal B-Environ*, 2018, 236: 326–337

13 Bazyari A, Khodadadi AA, Haghighat Mamaghani A, Beheshtian J, Thompson LT, Mortazavi Y. *Appl Catal B-Environ*, 2016, 180: 65–77

14 Wang H, Tang M, Shi F, Ding R, Wang L, Wu J, Li X, Liu Z, Lv B. *ACS Appl Mater Interfaces*, 2020, 12: 38140–38152

15 Chang X, Yang XF, Qiao Y, Wang S, Zhang MH, Xu J, Wang DH, Bu XH. *Small*, 2020, 16: 1906432

16 Astle MA, Rance GA, Loughlin HJ, Peters TD, Khlobystov AN. *Adv Funct Mater*, 2019, 29: 1808092

17 Zou J, Lin Y, Wu S, Wu M, Yang C. *Separation Purification Tech*, 2021, 264: 118434

18 Ye G, Gu Y, Zhou W, Xu W, Sun Y. *ACS Catal*, 2020, 10: 2384–2394

19 Smolders S, Willhammar T, Krajnc A, Sentosun K, Wharmby MT, Lomachenko KA, Bals S, Mali G, Roeffaers MBJ, De Vos DE, Bueken B. *Angew Chem Int Ed*, 2019, 58: 9160–9165

20 Willinger E, Massué C, Schlögl R, Willinger MG. *J Am Chem Soc*, 2017, 139: 12093–12101

21 Lin Y, Yang C, Niu Q, Luo S. *Adv Funct Mater*, 2022, 32: 2108814

22 Asif MB, Zhang S, Qiu L, Zhang Z. *Chem Catal*, 2022, 2: 550–562

23 Chen Y, Zhang G, Liu H, Qu J. *Angew Chem Int Ed*, 2019, 58: 8134–8138

24 Guo ZY, Li CX, Gao M, Han X, Zhang YJ, Zhang WJ, Li WW. *Angew Chem Int Ed*, 2021, 60: 274–280

25 Smith RDL, Prévot MS, Fagan RD, Zhang Z, Sedach PA, Siu MKJ, Trudel S, Berlinguette CP. *Science*, 2013, 340: 60–63

26 Chen W, Pei J, He CT, Wan J, Ren H, Zhu Y, Wang Y, Dong J, Tian S, Cheong WC, Lu S, Zheng L, Zheng X, Yan W, Zhuang Z, Chen C, Peng Q, Wang D, Li Y. *Angew Chem Int Ed*, 2017, 56: 16086–16090

27 Yang Y, Qian Y, Li H, Zhang Z, Mu Y, Do D, Zhou B, Dong J, Yan W, Qin Y, Fang L, Feng R, Zhou J, Zhang P, Dong J, Yu G, Liu Y, Zhang X, Fan X. *Sci Adv*, 2020, 6: eaba6586

28 Lee S, Lee YJ, Lee G, Soon A. *Nat Commun*, 2022, 13: 3171

29 Wu W, Niu C, Tian Q, Liu W, Niu G, Zheng X, Li C, Jia Y, Wei C, Xu Q. *Chem Commun*, 2020, 56: 14701–14704

30 Sun S, Sun Y, Zhou Y, Xi S, Ren X, Huang B, Liao H, Wang LP, Du Y, Xu ZJ. *Angew Chem Int Ed*, 2019, 58: 6042–6047

31 Chen K, Zhang XM, Yang XF, Jiao MG, Zhou Z, Zhang MH, Wang DH, Bu XH. *Appl Catal B-Environ*, 2018, 238: 263–273

32 Zhang X, Zhang Z, Zhang B, Yang X, Chang X, Zhou Z, Wang DH, Zhang MH, Bu XH. *Appl Catal B-Environ*, 2019, 256: 117804

33 Wang Z, Almatrafi E, Wang H, Qin H, Wang W, Du L, Chen S, Zeng G, Xu P. *Angew Chem Int Ed*, 2022, 61: e202202338